

A novel engineered oxide buffer approach for fully lattice-matched SOI heterostructures

A Giussani^{1,3}, P Zaumseil¹, O Seifarth¹, P Storck² and T Schroeder¹

¹ IHP, Im Technologiepark 25, 15236 Frankfurt (Oder), Germany

² Siltronic AG, Hanns-Seidel-Platz 4, 81737 München, Germany

E-mail: giussani@ihp-microelectronics.com

New Journal of Physics **12** (2010) 093005 (12pp)

Received 27 May 2010

Published 6 September 2010

Online at <http://www.njp.org/>

doi:10.1088/1367-2630/12/9/093005

Abstract. Epitaxial (epi) oxides on silicon can be used to integrate novel device concepts on the canonical Si platform, including functional oxides, e.g. multiferroics, as well as alternative semiconductor approaches. For all these applications, the quality of the oxide heterostructure is a key figure of merit. In this paper, it is shown that, by co-evaporating Y_2O_3 and Pr_2O_3 powder materials, perfectly lattice-matched $PrYO_3(111)$ epilayers with bixbyite structure can be grown on Si(111) substrates. A high-resolution x-ray diffraction analysis demonstrates that the mixed oxide epi-films are single crystalline and type B oriented. Si epitaxial overgrowth of the $PrYO_3(111)/Si(111)$ support system results in flat, continuous and fully lattice-matched epi-Si(111)/ $PrYO_3(111)/Si(111)$ silicon-on-insulator heterostructures. Raman spectroscopy proves the strain-free nature of the epi-Si films. A Williamson–Hall analysis of the mixed oxide layer highlights the existence of structural defects in the buffer, which can be explained by the thermal expansion coefficients of Si and $PrYO_3$.

³ Author to whom any correspondence should be addressed.

Contents

1. Introduction	2
2. Experimental	3
3. Results and discussion	4
4. Conclusions and outlook	10
Acknowledgment	11
References	11

1. Introduction

In the recent past, crystalline oxides on silicon (COSs) have been widely investigated as functional materials and epitaxial (epi) templates for microelectronic and optoelectronic applications. As functional layers, for instance, perovskite, e.g. SrTiO₃ (STO) [1], and pyrochlore, e.g. La₂Zr₂O₇ [2], high-*k* dielectrics were successfully grown by molecular beam epitaxy (MBE) on Si(001) and Si(111), respectively, with the aim of replacing SiO₂ in silicon complementary metal oxide semiconductor technology (CMOS). Previous efforts have also focused on the implementation of epitaxial perovskite Pb(Zr_x, Ti_{1-x})O₃ (PZT) layers on STO/Si substrates with SrRuO₃ bottom electrodes in a probe-based data storage concept, based on the Millipede idea developed by IBM [3]–[5], to develop ferroelectric random access memories (FRAMs) [6]. Moreover, PZT thin films deposited on Si(001) wafers with STO/MgO as the buffer layer system and YBa₂Cu₃O₇ (YBCO) as the electrode were successfully prepared by pulse laser deposition (PLD) for ferroelectric film micro-electro-mechanical system (MEMS) devices [7]. COSs have also been considered as templates for the integration of alternative semiconductors on the Si platform. Crack-free, wide-bandgap semiconducting ZnO epi-films on Si(111) were accomplished by PLD using either bixbyite Lu₂O₃ [8] or Sc₂O₃ [9] intervening layers, paving the way to the incorporation of ZnO-based optoelectronic functions into Si electronics [10]. Perovskite Sr(Hf, Ti)O₃ [11] and bixbyite cubic (cub)-Pr₂O₃ [12] were studied for the realization of germanium-on-insulator (GeOI) heterostructures on Si, whereas bixbyite Gd₂O₃ was examined as a lattice mediator to monolithically combine the optoelectronic properties of InP with Si technology [10]. The growth of epi-Si on epi-oxide/Si support systems is being pursued as well to build up Si-based resonant tunneling devices, e.g. epi-Si/Ce₂O₃/Si(111) [13] and epi-Si/Gd₂O₃/Si(111) [14], and silicon-on-insulator (SOI) substrates for high-performance CMOS applications, e.g. epi-Si/ γ -Al₂O₃/Si(001) [15, 16], epi-Si/Y₂O₃/Pr₂O₃/Si(111) [17], epi-Si/Y₂O₃/Si(111) [18, 19] and epi-Si/(La_xY_{1-x})₂O₃/Si(111) [20]–[22].

Major issues in heteroepitaxy are (i) lattice and thermal mismatch between the film and the substrate, often resulting in unacceptable defect densities and/or cracking; (ii) difference in energetics between the epilayer and the substrate, determining the wetting or non-wetting behavior of the former; and (iii) thermodynamical instability of the epi-film in contact with the substrate. An interesting example, which illustrates challenges (a) and (c), is provided by the above-mentioned epi-Si/(La_xY_{1-x})₂O₃/Si(111) heterostructure. The ternary oxide was deposited by MBE, using molecular oxygen and thermally evaporated La and Y with the target to achieve a layer lattice matched to the Si substrate. It was demonstrated that, by incorporating a small amount of La (larger atomic radius) into the growing bixbyite Y₂O₃ film, the lattice mismatch of -2.4% between Y₂O₃ and Si could be changed to $+0.18\%$ for $x = 0.29$. However,

one disadvantage of the $(\text{La}_x\text{Y}_{1-x})_2\text{O}_3$ system is that the lattice window accessible is limited to $x \sim 0.35$. For higher La concentrations, phase separation occurs, with formation of hexagonal La_2O_3 domains in the main cubic Y_2O_3 matrix [22].

In the present paper, it is proven that an epitaxial insulator perfectly lattice matched to Si(111) can be obtained by MBE by suitably mixing isomorphous oxides, Y_2O_3 and Pr_2O_3 , in their cubic phase. Both these oxides indeed crystallize in the bixbyite structure, which can be thought of as an oxygen-deficient fluorite, where the lattice parameter is doubled and an ordered oxygen vacancy superstructure exists by removing a quarter of the oxygen atoms [23, 24]. The Y_2O_3 and cub- Pr_2O_3 lattice constants are 2.4% smaller ($a_{\text{Y}_2\text{O}_3} = 1.604 \text{ nm}$) and 2.7% bigger ($a_{\text{cub-Pr}_2\text{O}_3} = 1.1152 \text{ nm}$) than twice the Si lattice parameter ($a_{\text{Si}} = 0.5430 \text{ nm}$), respectively. By controlling the co-evaporation of the Y_2O_3 and Pr_2O_3 sources and the deposition temperature, the $(\text{Pr}_x\text{Y}_{1-x})_2\text{O}_3$ ternary system can span the complete lattice window $0 < x < 1$ without running into phase separation, matching the room temperature (RT) Si lattice constant for $x = 0.47$ (hereafter, the Si-lattice-matched mixed oxide is denoted as PrYO_3 for the sake of simplicity). In addition, it is shown that an epi-Si/ PrYO_3 /Si(111) SOI heterostructure characterized as fully lattice matched at RT is not necessarily free from structural defects. High-temperature measurements demonstrate that a more complex treatment, taking the different thermal expansion coefficients of oxide and the Si substrate into account, is required to obtain optimized buffer layers.

2. Experimental

Four-inch B-doped Si(111) wafers ($\rho = 5\text{--}15 \Omega \text{ cm}$) were wet-cleaned according to a standard recipe, recently reported in detail [25]. Loaded onto the DCA 600 MBE machine, samples were first annealed at 700°C for 5 min in ultra high vacuum (UHV) (base pressure 10^{-10} mbar) to prepare high-quality (7×7) Si(111) reconstructed surfaces. Then epi-oxide thin films were deposited by simultaneous electron beam evaporation of Y_2O_3 and Pr_2O_3 powder materials from pyrolytic graphite crucibles at a substrate temperature of 780°C and a growth rate of 0.1 nm s^{-1} . Tuning the $\text{Y}_2\text{O}_3/\text{Pr}_2\text{O}_3$ ratio resulted in $(\text{Pr}_x\text{Y}_{1-x})_2\text{O}_3$ films with about $x = 0.5$, as estimated by XPS measurements [26]. The PrYO_3 oxide was then overgrown with epitaxial Si at a substrate temperature of 625°C and a growth rate of 0.02 nm s^{-1} . The thickness and roughness of the epilayers composing the heterostructures were measured by x-ray reflectivity (XRR) (not shown). Samples were extensively investigated by x-ray diffraction (XRD) techniques. A Rigaku DMAX 1500 instrument equipped with Cu K_α radiation was employed for specular $\theta\text{--}2\theta$ scans, whereas a Kappa-Six circle diffractometer was used at the ID 32 beamline of the European Synchrotron Radiation Facility (ESRF) in Grenoble for synchrotron radiation grazing incident x-ray diffraction (SR-GIXRD) measurements. Here, a beam energy of 10.6 keV was selected, resulting in critical angles α_c of 0.17° , 0.22° , and 0.26° for total reflection at the Si, Y_2O_3 and Pr_2O_3 surfaces, respectively. SR-GIXRD in-plane scans are recorded in the following with respect to the Si(111) surface unit cell of hexagonal symmetry (indicated by the apex S) [27]. However, for the sake of simplicity, Bragg peaks are also labeled with respect to the bulk cubic unit cells of Si, Pr_2O_3 and Y_2O_3 . High-resolution ϕ -scans and high-temperature specular $\theta\text{--}2\theta$ scans were performed by means of a Rigaku SmartLab diffractometer with a Cu K_α source. Finally, Raman spectroscopy was applied to characterize the top epi-Si layers. It is a powerful tool to assess the extent of strain in semiconducting materials, since it is non-destructive, does not require sample preparation, provides a quick response and allows us to

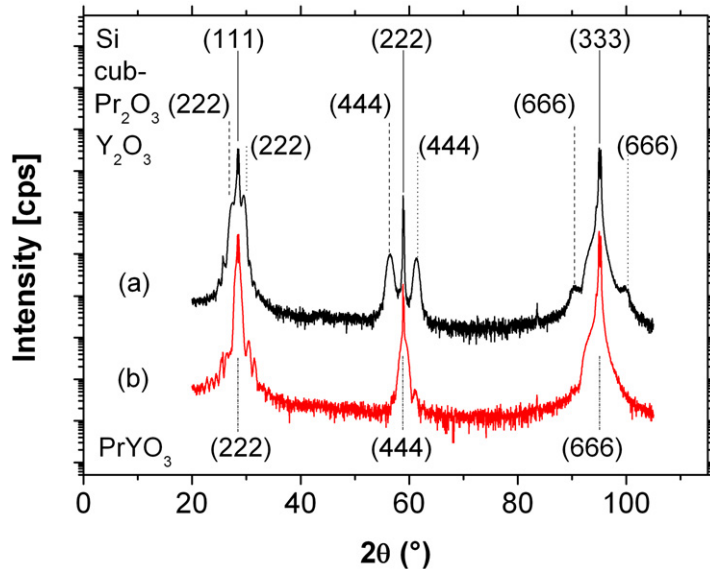


Figure 1. XRD specular θ - 2θ scan of (a) an epi-Si/ Y_2O_3 /cub- Pr_2O_3 /Si(111) heterostructure and (b) an epi-Si/ PrYO_3 /Si(111) system.

vary the analysis depth by tuning the laser wavelength [28]. An Invia Renishaw equipment with a wavelength of 364 nm was utilized to confine the excitation within the Si epilayers (the probing depth is about 12 nm).

The structural characterization of the epi-Si/ PrYO_3 /Si(111) system is presented in the following section. For reference, the corresponding data of epi-Si/ Y_2O_3 /cub- Pr_2O_3 /Si(111) heterostacks, widely described in [26], are included in the figures.

3. Results and discussion

Figure 1 shows the XRD specular θ - 2θ scans for a 70 nm epi-Si/10 nm Y_2O_3 /10 nm cub- Pr_2O_3 /Si(111) specimen (figure 1(a)) and a 70 nm epi-Si/10 nm PrYO_3 /Si(111) system (figure 1(b)). For the former, together with the Si(111), (222) and (333) Bragg peaks from the Si substrate at the expected positions $2\theta = 28.45^\circ$, 58.87° , and 94.97° , respectively, cub- Pr_2O_3 (222), (444) and (666) reflections at $2\theta = 27.32^\circ$, 56.48° and 90.26° and Y_2O_3 (222), (444) and (666) peaks at $2\theta = 29.48^\circ$, 61.31° , and 99.92° are observed. The double peak structure of the oxide bilayer is best seen by focusing on the 2θ interval around the kinematically quasi-forbidden Si(222) reflection. Analysis of the oxide peak positions reveals that, in the vertical direction, the cub- Pr_2O_3 and Y_2O_3 lattice parameters are about 1.2% bigger and smaller, respectively, than the corresponding bulk lattice constants (e.g. the experimental 2θ for cub- Pr_2O_3 (444) is 56.48° versus the 57.18° bulk value, and the experimental 2θ for Y_2O_3 (444) is 61.31° versus the 60.44° bulk value). This result is in agreement with a recent *in situ* RHEED-XPS study of strain relaxation in Y_2O_3 epi-films on cub- Pr_2O_3 /Si(111) support systems, from which it was revealed that tensile strain in the Y_2O_3 epilayer is accommodated gradually with increasing Y_2O_3 thickness [29]. No additional Bragg peaks are detected in figure 1(a), in line with the presence of a fully relaxed Si top epilayer whose reflections overlap the ones from the Si substrate. Differently, in the case of the epi-Si/ PrYO_3 /Si(111) heterostack (figure 1(b)), only

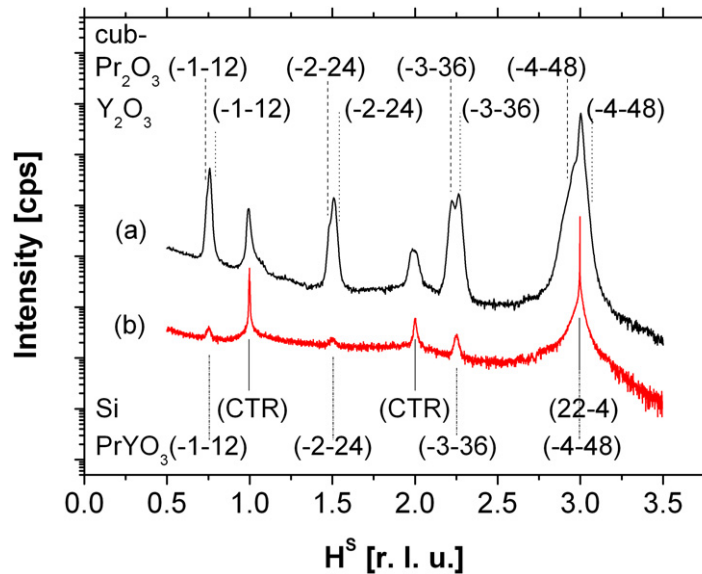


Figure 2. SR-GIXRD in-plane scans along $[100]^S$ ($[1\ 1\ -2]$) with $L^S = 0.05$ rlu and $\alpha = 0.6^\circ$ for (a) the epi-Si/ Y_2O_3 /cub- Pr_2O_3 /Si(111) heterostructure and (b) the epi-Si/ $PrYO_3$ /Si(111) system.

three peaks are detected at the 2θ values of Si(111), (222) and (333). This indicates that the $PrYO_3$ mixed oxide and the epi-Si film have the same vertical (111) orientation and exactly the same lattice constant as the Si substrate. The fringes around the Si(111) and Si(222) reflections were caused by interference effects between the oxide epilayer and the Si substrate, which have different scattering powers. From their spacing it is possible to estimate the thickness of the $PrYO_3$ film, which turns out to be about 8 nm, in line with the XRR analysis. It is worth noting that, whereas the deposition of Pr oxide on Si(111) at temperatures around $600^\circ C$ results in the growth of the non-thermodynamically stable hexagonal Pr_2O_3 phase, owing to the low lattice-misfit with Si(111) [30, 31], no hexagonal features are detected in the mixed cubic oxide film. This points to a stabilization of the cub-Pr oxide phase by Y oxide admixture. The specular $\theta-2\theta$ results are confirmed by the SR-GIXRD analysis. In-plane scans were performed along the $H^S = [100]^S$ direction (corresponding to $[1\ 1\ -2]$ in bulk coordinates) for $L^S = 0.05$ and with an incident angle α of 0.6° , therefore probing the whole heterostructure (figure 2). The curve in figure 2(a) reports the spectrum for the epi-Si/ Y_2O_3 /cub- Pr_2O_3 /Si(111) specimen. Two Si crystal truncation rods (CTRs) at $H^S = 1$ and 2 rlu (reciprocal lattice unit) and an Si(22-4) Bragg peak at $H^S = 3$ rlu are seen, originating from the Si(111) substrate and the Si(111) epilayer, the latter causing a broadening of the sharp substrate reflections. Moreover, cub- $Pr_2O_3(-1\ -1\ 2)$, $(-2\ -2\ 4)$ and $(-3\ -3\ 6)$ Bragg peaks at $H^S = 0.74$, 1.48 and 2.22 rlu, respectively (bulk values $H^S = 0.73$, 1.46 and 2.19 rlu), and $Y_2O_3(-1\ -1\ 2)$, $(-2\ -2\ 4)$ and $(-3\ -3\ 6)$ Bragg peaks at $H^S = 0.76$, 1.52 and 2.27, respectively (bulk values $H^S = 0.77$, 1.54 and 2.30 rlu), are clearly visible. Instead, the cub- $Pr_2O_3(-4\ -4\ 8)$ and $Y_2O_3(-4\ -4\ 8)$ reflections are more difficult to analyze, owing to the close Si(22-4) Bragg peaks from the Si substrate and the Si epilayer at $H^S = 3$ rlu. Comparing the experimental oxide peak positions with the theoretical bulk ones, it turns out that, along $[1\ 1\ -2]$, cub- Pr_2O_3 is in-plane compressively strained by about 1.3% due to the influence of the smaller

Si lattice underneath (experimental $\{112\}$ d -spacing $d_{112}(\text{cub-Pr}_2\text{O}_3) = 4.493$ nm versus bulk $d_{112}(\text{cub-Pr}_2\text{O}_3) = 4.553$ nm), whereas Y_2O_3 is in-plane tensely strained by about 1.5% owing to the bigger cub- Pr_2O_3 lattice underneath and epi-Si lattice on top (experimental $d_{112}(\text{Y}_2\text{O}_3) = 4.395$ nm versus bulk $d_{112}(\text{Y}_2\text{O}_3) = 4.329$ nm). Analogous results were obtained along the other high symmetry direction $H^S = K^S = [110]^S$ ($[01-1]$ in bulk coordinates) (not shown). The scan of figure 2(b) presents the SR-GIXRD scan along $H^S = [100]^S$, with H^S ranging from 0.5 to 3.5 rlu for the epi-Si/ PrYO_3 /Si(111) system. As expected, two CTRs and the Si(22-4) Bragg peak from the Si(111) epi-film and the Si(111) substrate are found at $H^S = 1, 2$ and 3 rlu, respectively. Three additional reflections show up at $H^S = 0.75, 1.5$ and 2.25 rlu, which can be assigned to the PrYO_3 mixed oxide with bixbyite structure, namely $\text{PrYO}_3(-1-12)$, $(-2-24)$ and $(-3-36)$, respectively. Interestingly, the calculated d -spacing of the $\{112\}$ netplanes in PrYO_3 is $d_{112}(\text{PrYO}_3) = 0.2217$ nm, which is exactly the d -spacing of the $\{112\}$ netplanes in the Si lattice. This means that the PrYO_3 oxide buffer is in-plane perfectly lattice matched to the Si substrate. For this reason, the $\text{PrYO}_3(-4-48)$ Bragg peak fully coincides with the Si(22-4) Bragg peak at $H^S = 3$ rlu. Furthermore, since no extra reflections are detected, it is concluded that the top epi-Si layer is also lattice matched to the underlying $\text{PrYO}_3(111)$ /Si(111) support system (consistent results were deduced scanning along $[110]^S$ (not shown)). The structural difference between the $\text{Y}_2\text{O}_3/\text{Pr}_2\text{O}_3$ and the PrYO_3 buffers is best seen by considering figures 3(a) and (b), which report the in-plane (H-K) reciprocal space maps (RSMs), taken with $L^S = 0.05$ rlu and $\alpha = 0.6^\circ$, of the $\text{Y}_2\text{O}_3(-3-36)/\text{cub-Pr}_2\text{O}_3(-3-36)$ and $\text{PrYO}_3(-3-36)$ Bragg peaks, respectively. It is clear that, whereas a double peak is observed in the case of the bilayer buffer, a single and homogeneous $(-3-36)$ Bragg peak is recorded for the mixed oxide. In the same way, RSMs were also recorded around the $\text{PrYO}_3(-2-24)$ and $(-1-12)$ Bragg peaks for the epi-Si(111)/ $\text{PrYO}_3(111)$ /Si(111) heterostructure (figures 3(c) and (d), respectively). A Williamson-Hall (W-H) analysis [32] of the $\text{PrYO}_3(-n-n2n)$ reflections ($n = 1, 2, 3$) was performed and the results are shown in figure 4. The full-width at half-maximum (FWHM) of each peak was extracted from the respective RSM along the two in-plane high-symmetry directions $[100]^S$ and $[110]^S$ and was plotted versus the H^S position of the peak. Afterwards, a linear regression of the two curves was executed. An in-plane PrYO_3 domain size of about 13 nm along $[100]^S$ and $[110]^S$ was calculated from the line intercepts. Moreover, from the slopes of the FWHM($[110]^S$) and FWHM($[100]^S$) curves, respectively, an in-plane mosaicity of about 0.4° and in-plane strain variation of about 1% were estimated. Hence, the W-H study reveals that, although the oxide buffer is perfectly lattice matched to the Si substrate, it is not free from structural defects causing lattice micro-strain and tilt and limiting the long-range order. A point will be made on that at the end of the section.

The anti-parallel indexing of the in-plane Si and oxide Bragg peaks is applied, due to the so-called type-B stacking configuration of ionic insulator heterostructures on Si(111) [17]. Here, it is recalled that a type-B (111)-oriented face centered cubic (fcc) epilayer has its stacking vector rotated by 180° around $[111]$ with respect to the type-A stacking vector of the Si(111) substrate [33]. Although it is well known that the $\text{Y}_2\text{O}_3(111)/\text{cub-Pr}_2\text{O}_3(111)$ bilayer buffer grows on Si(111) in a type-B fashion [17], the stacking configuration of the (111) netplanes of the $\text{PrYO}_3(111)$ epi-film on Si(111) still needs to be determined. For this reason, ϕ scans on the $\{400\}$ and $\{200\}$ families of planes were performed for the fully lattice-matched epi-Si/ PrYO_3 /Si(111) specimen (figure 5). The ϕ scan on (400), which is allowed for both the diamond Si lattice and the bixbyite PrYO_3 one, shows a group of three intense Bragg peaks at $\phi = 90^\circ, 210^\circ$ and 330° and three weaker features at $\phi = 30^\circ, 150^\circ$ and 270°

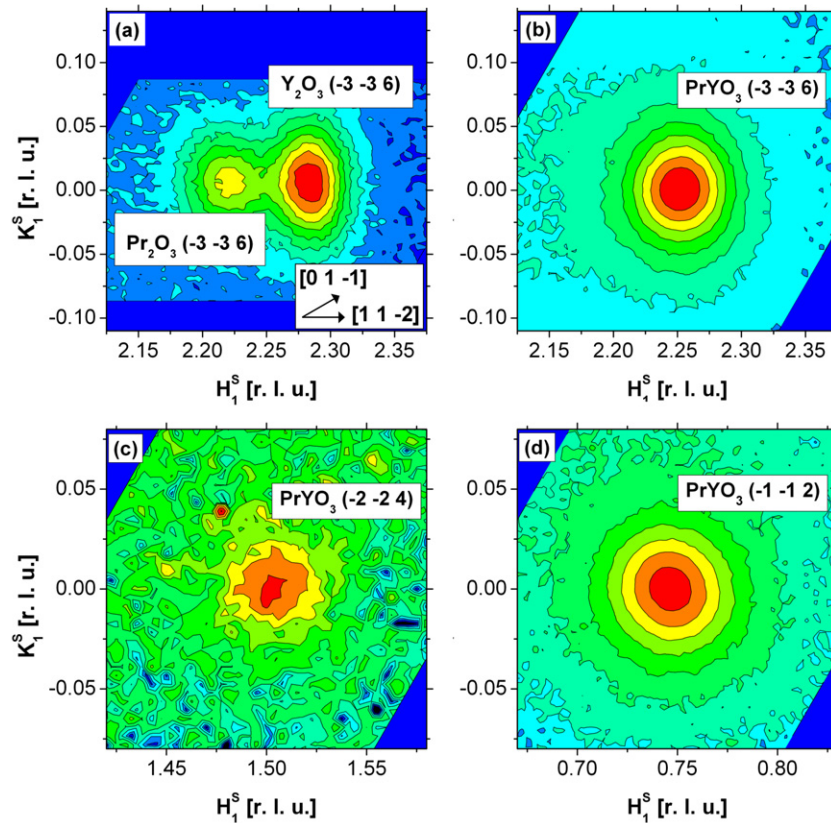


Figure 3. SR-GIXRD RSMs around (a) the $\text{Y}_2\text{O}_3(-3 -3 6)/\text{cub-Pr}_2\text{O}_3(-3 -3 6)$ Bragg peak and (b)–(d) the $\text{PrYO}_3(-n -n 2n)$ Bragg peaks ($n = 3, 2, 1$, respectively). The Cartesian coordinate system is defined as $H_1^S = H^S + K^S/2$; $K_1^S = K^S \cdot \sqrt{3}/2$. The H^S and $H^S = K^S$ ($[1 1 -2]$ and $[0 1 -1]$ in bulk coordinates, respectively) are depicted in the inset of panel (a). The logarithmic intensity scales are (a) $10\text{--}10^4$ cps, (b) $10\text{--}280$ cps, (c) $30\text{--}8.5 \times 10^3$ cps and (d) $50\text{--}1.5 \times 10^3$ cps. $L^S = 0.05$ rlu and $\alpha = 0.6^\circ$.

(figure 5(a)). The former set of reflections mainly originates from the semi-infinite Si(111) substrate with type-A orientation, whereas the latter group of Bragg peaks clearly indicates the presence of some type-B orientation in the heterostructure. In contrast, the ϕ scan on the (200) Bragg peak, which is allowed only for the bixbyite structure, exhibits only three reflections at $\phi = 30^\circ, 150^\circ$ and 270° (figure 5(b)). It is concluded that the Si lattice-matched PrYO_3 oxide layer has its (111) netplanes oriented according to a type-B stacking configuration and it is free from rotational twins. Combining the data of figure 6 with the in-plane measurements of figure 2, the heterostructure azimuthal orientation can be assigned, resulting in $\text{epi-Si}[1 1 -2] \parallel \text{PrYO}_3[-1 -1 2] \parallel \text{Si}[1 1 -2]$.

Finally, the Si–Si Raman vibration line of about 20 nm-thick Si(111) epilayers grown on a 10 nm $\text{PrYO}_3/\text{Si}(111)$ support system and on a 10 nm $\text{Y}_2\text{O}_3/10$ nm $\text{cub-Pr}_2\text{O}_3/\text{Si}(111)$ heterostructure, respectively, were compared, as illustrated in figure 6. As a reference, the Si–Si Raman line of a bare Si(111) wafer was also measured (solid curve (a)) and its position and width were found to be 520.5 and 3.3 cm^{-1} , respectively. It is seen that the Si–Si line for the

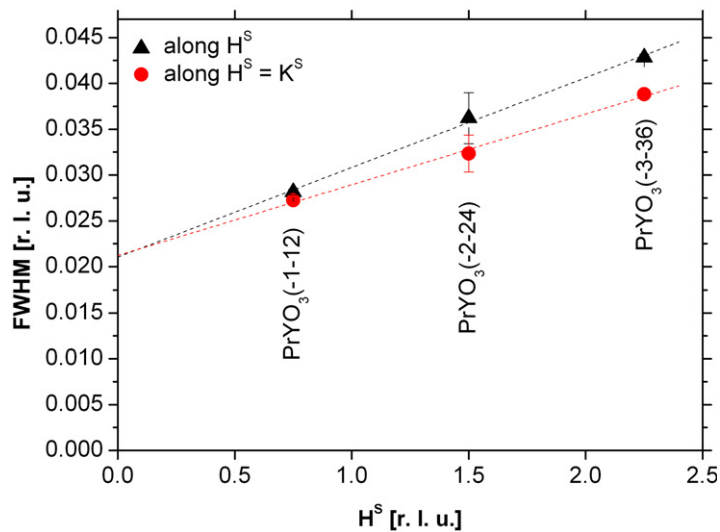


Figure 4. W–H plot analysis of the $\text{PrYO}_3(-n -n 2n)$ Bragg peaks ($n = 1-3$). Slope and intercept of the curve linear regression resulted in 0.01 ± 0.001 and 0.021 ± 0.001 rlu along H^S (triangles) and 0.008 ± 0.001 and 0.021 ± 0.001 rlu $H^S = K^S$ (circles), respectively.

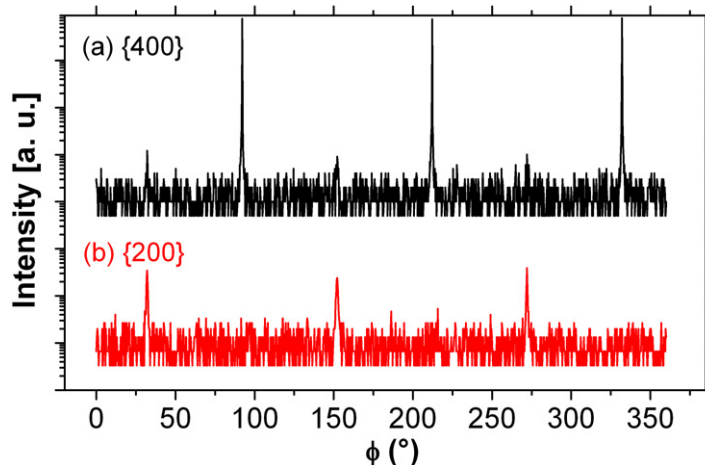


Figure 5. The ϕ scans with $\alpha = 0.6^\circ$ on (a) $\{400\}$ and (b) $\{200\}$ Bragg peaks. During the scans, the sample is rotated over a range of 360° around its surface normal ($[00L]^S = [111]$) while keeping the Bragg–Brentano diffraction condition satisfied for either $\text{Si}\{200\}$ or $\text{Si}\{400\}$ (see [38] for details about ϕ scans).

$\text{Si}(111)$ epilayer deposited on the mixed oxide (dashed curve (b)) is symmetric and has within the error limits the same position (520.6 cm^{-1}) as the substrate feature, indicating that the epi-Si deposited on the Si-lattice-matched PrYO_3 buffer is not strained. However, curve (b) is wider (4.1 cm^{-1}) than curve (a), pointing to the presence of structural defects in the epi-Si film, in agreement with the limited long-range order of the mixed oxide buffer. The Raman peak of the epi-Si film grown on the bilayer heterostructure (dashed dotted curve (c)) is asymmetric

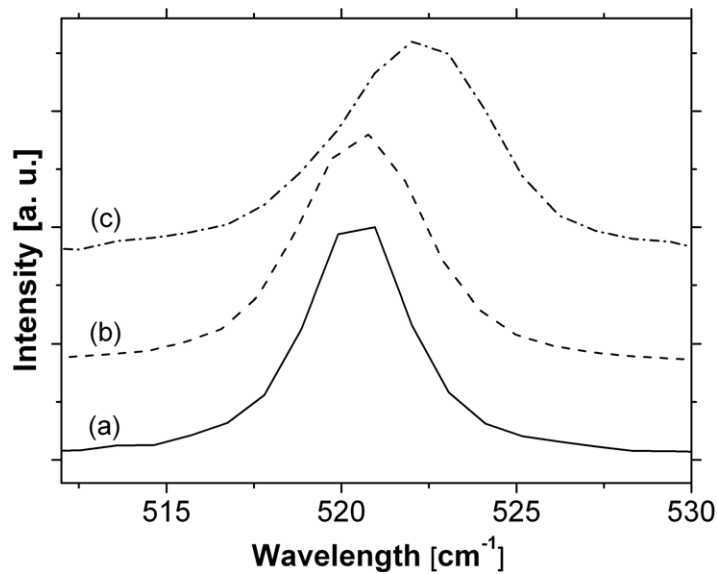


Figure 6. Si–Si Raman spectra of (a) a bare Si(111) reference wafer (solid curve), (b) a 20 nm epi-Si(111)/10 nm PrYO₃(111)/Si(111) system (dashed curve) and (c) a 20 nm epi-Si(111)/10 nm Y₂O₃(111)/10 nm cub-Pr₂O₃(111)/Si(111) heterostructure (dash-dotted curve).

with a position of 522.1 cm^{-1} and is much broader (4.9 cm^{-1}) than the Si(111) substrate line. The shift of the Raman line reveals in-plane compressive strain in the epi-Si film, whereas peak asymmetry and broadening are attributable to inhomogeneous strain distribution along the layer thickness and/or structural defects, as recently outlined for epi-Si layers on SiGe virtual substrates [28].

The fact that the PrYO₃ lattice is perfectly matched to the Si substrate while exhibiting structural imperfection, as unveiled by the W–H analysis, seems to be contradictory. However, it has to be kept in mind that the XRD analyses were performed at RT. To figure out what happens during the epitaxial process at 780°C , high-resolution θ – 2θ scans were performed around the Si(111) and Si(222) reflections at temperatures up to 725°C under an N₂ atmosphere. The measured lattice constants in the direction normal to the wafer surface (a_{\perp}) are shown in figure 7 for the Si substrate and the 10 nm-thick PrYO₃ layer (any signal from the epi-Si layer is completely superimposed by the much stronger Si substrate reflection). At RT, the a_{\perp} parameters of Si and PrYO₃ are nearly equal according to the matched lattice. However, with increasing temperature, the a_{\perp} lattice constant of the mixed oxide increases much faster than that of Si. The main reason for this stronger increase is a significantly larger coefficient of thermal expansion of the oxide. As long as no plastic deformation occurs, the in-plane lattice constant of the oxide is fixed to that of the Si substrate and follows the expansion of Si with increasing temperature. Since the oxide expands more than the Si substrate, this leads to a tetragonal distortion of the oxide lattice, with the oxide a_{\perp} lattice parameter expanding faster than expected for the bulk values as the temperature rises. The oxide point at 50°C was measured after heating the sample to 725°C and then cooling it down. The fact that this point is very close to lattice constant values measured during the ramp-up from RT to 725°C indicates that no significant additional relaxation occurred during the high-temperature

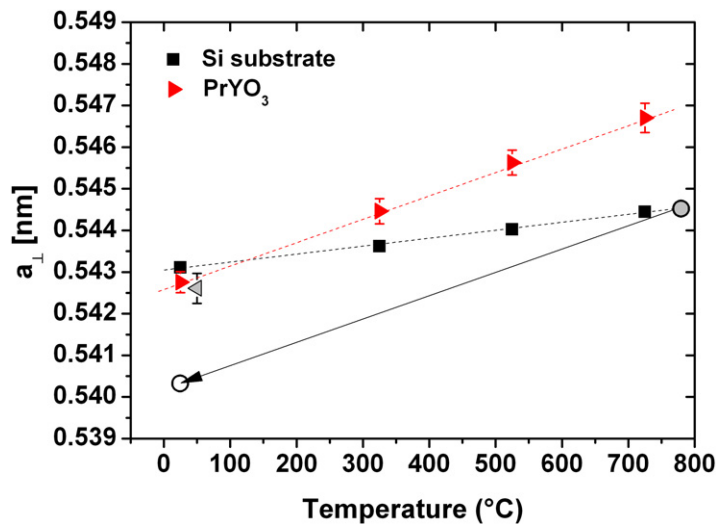


Figure 7. The a_{\perp} lattice constants of the Si substrate (squares) and the half a_{\perp} lattice constants of PrYO_3 (triangles) measured in the temperature range $25^{\circ}\text{C} < T < 725^{\circ}\text{C}$. Full and empty circles represent estimated half a_{\perp} lattice constants at 780°C and at RT, respectively, for a $(\text{Pr}_x\text{Y}_{1-x})_2\text{O}_3$ epilayer lattice matched to Si at the growth temperature of 780°C .

experiment. The trend of the lattice constants versus temperature is approximated in figure 7 by linear behavior, neglecting any temperature dependence of the expansion coefficients. It is evident that there exists a significant difference (0.0024 nm) between the a_{\perp} lattice constants of the two materials at the oxide deposition temperature of 780°C . The mixed oxide layer of the given stoichiometry is obviously strained at the growth temperature and it probably relaxes plastically by the generation of misfit dislocations, which are responsible for the measured mosaicity and micro-strain. In order to increase the long-range order of the mixed oxide, it is therefore important that lattice matching is achieved at the growth temperature (full circle in figure 7) rather than at RT. To do that, the stoichiometry of the $(\text{Pr}_x\text{Y}_{1-x})_2\text{O}_3$ has to be changed towards the Y_2O_3 side (smaller x values). Cooling this structure down to RT would then result in an oxide a_{\perp} lattice constant of about 0.5403 nm (the arrow and the empty circle in figure 7). This means that an oxide lattice with a well-defined mismatch at RT must be the goal for further improvement of the epilayer quality.

4. Conclusions and outlook

It was shown that, by electron gun co-evaporation of Pr_2O_3 and Y_2O_3 sources, it is feasible to grow $(\text{Pr}_x\text{Y}_{1-x})_2\text{O}_3$ epilayers on Si(111) that are perfectly lattice matched at RT. The PrYO_3 epi-films are (111) oriented and single crystalline and exhibit a type-B stacking configuration. At the deposition temperature of 780°C , the cubic bixbyite structure is the thermodynamically stable phase of both Pr_2O_3 and Y_2O_3 . Therefore, no phase separation occurs within the mixed oxide. This means that the $(\text{Pr}_x\text{Y}_{1-x})_2\text{O}_3$ lattice constant can be tuned without any restriction, and especially in the range $0.47 < x < 1$ it is possible to fit the lattice parameter of SiGe alloys up to $\text{Si}_{0.2}\text{Ge}_{0.8}$ [34]. This is clearly an advantage compared to the $(\text{La}_x\text{Y}_{1-x})_2\text{O}_3$ system.

In this case, indeed, La-rich hexagonal domains start nucleating at 600 °C within the cubic matrix for La content $x > 0.35$, owing to the fact that, at high temperature, hex- La_2O_3 and not cub- La_2O_3 is the stable phase. Furthermore, on the $\text{PrYO}_3(111)/\text{Si}(111)$ support system, single crystalline, type-A-oriented epi-Si(111) films could be grown, achieving fully lattice-matched and unstrained epi-Si(111)/ $\text{PrYO}_3(111)/\text{Si}(111)$ heterostructures with azimuthal orientation given by epi-Si[1 1 -2]|| $\text{PrYO}_3[-1 -1 2]$ ||Si[1 1 -2].

However, the PrYO_3 domain size is rather limited (13 nm). An explanation for this phenomenon was provided by temperature-dependent XRD measurements. At the elevated growth temperature of 780 °C, PrYO_3 grows in a strained state, and misfit dislocations are probably generated at the $\text{PrYO}_3/\text{Si}(111)$ substrate interface, limiting in this way the long-range order of the oxide crystallinity. Experiments are ongoing to tune the $(\text{Pr}_x\text{Y}_{1-x})_2\text{O}_3$ epi-film stoichiometry so that lattice match of the mixed oxide to Si is achieved at the oxide growth temperature instead of at RT. It is then expected that the mixed oxide structural quality will be superior to that of the presented specimen. As a result of high-temperature XRD investigations, an optimization of the growth recipe is ongoing in parallel with further XRD/TEM studies of the film defect structure to gain a deeper understanding of the factors limiting the lateral size of the mixed oxide domains. Finally, grazing incidence x-ray absorption fine-structure (XAFS) experiments at the Y K- and Pr L₃-absorption edges are planned in order to determine whether the mixed oxide exhibits random atomic-scale ordering or whether there is a preference for or against cation clustering [35]–[37]. Such studies could trigger the development of Eu : $(\text{Pr}_x\text{Y}_{1-x})_2\text{O}_3$ films as scintillator materials. To optimize the optical activity, it is indeed fundamental that the Eu^{3+} activator cations reside solely on the non-centrosymmetric C₂ cation sites of the $(\text{Pr}_x\text{Y}_{1-x})_2\text{O}_3$ bixbyite crystal, which in principle offers two non-equivalent cation sites with different point group symmetries (C₂ and S₆) [23]. In general, the development of engineered oxide heterostructures with tailored properties (e.g. lattice constant) will pave the way for the integration of novel oxide and semiconductor device concepts in Si nanoelectronics.

Acknowledgment

The authors are grateful to the following organizations for funding and infrastructure support: the DFG, Siltronic AG and the ESRF.

References

- [1] McKee R A, Walker F J and Chisholm M F 1998 *Phys. Rev. Lett.* **81** 3014
- [2] Seo J W, Fompeyrine J, Guiller A, Norga G, Marchiori C, Siegwart H and Locquet J P 2003 *Appl. Phys. Lett.* **83** 5211
- [3] Vettiger P *et al* 2002 *IEEE Trans. Nanotechnol.* **1** 39
- [4] 2005 *III-Vs Rev.* **18** 24
- [5] 2002 *Mater. Today* **5** 7
- [6] Martin L W, Chu Y H and Ramesh R 2010 *Mater. Sci. Eng. R* **68** 89
- [7] Zhao J, Lu L, Thompson C V, Lu Y F and Song W D 2001 *J. Cryst. Growth* **225** 173
- [8] Guo W, Allenic A, Chen Y B, Pan X Q, Tian W, Adamo C and Schlom D G 2008 *Appl. Phys. Lett.* **92** 072101
- [9] Guo W, Katz M B, Nelson C T, Heeg T, Schlom D G, Liu B, Che Y and Pan X Q 2009 *Appl. Phys. Lett.* **94** 122107
- [10] Saint-Girons G, Regreny P, Largeau L, Patriarche G and Hollinger G 2007 *Appl. Phys. Lett.* **91** 241912

- [11] Seo J W *et al* 2007 *Microelectron. Eng.* **84** 2328
- [12] Giussani A, Rodenbach P, Zaumseil P, Dabrowski J, Kurps R, Weidner G, Mussig H J, Storck P, Wollschläger J and Schroeder T 2009 *J. Appl. Phys.* **105** 033512
- [13] Jones J T, Croke E T, Garland C M, Marsh O J and McGill T C 1998 *J. Vac. Sci. Technol. B* **16** 2686
- [14] Fissel A, Kühne D, Bugiel E and Osten H J 2006 *J. Vac. Sci. Technol. B* **24** 2041
- [15] Ishida M, Katakabe I, Nakamura T and Ohtake N 1988 *Appl. Phys. Lett.* **52** 1326
- [16] Ishida M, Yamaguchi S, Masa Y, Nakamura T and Hikita Y 1991 *J. Appl. Phys.* **69** 8408
- [17] Schroeder T, Zaumseil P, Seifarth O, Giussani A, Müssig H J, Storck P, Geiger D, Lichte H and Dabrowski J 2008 *New J. Phys.* **10** 113004
- [18] Elmasry N A, Hunter M, ElNaggar A and Bedair S M 2005 *J. Appl. Phys.* **98** 106104
- [19] Borschel C, Ronning C, Hofsass H, Giussani A, Zaumseil P, Wenger C, Storck P and Schroeder T 2009 *J. Vac. Sci. Technol. B* **27** 305
- [20] Guha S, Bojarczuk N A and Narayanan V 2002 *Appl. Phys. Lett.* **80** 766
- [21] Bojarczuk N A, Copel M, Guha S, Narayanan V, Preisler E J, Ross F M and Shang H 2003 *Appl. Phys. Lett.* **83** 5443
- [22] Narayanan V, Guha S, Bojarczuk N A and Ross F M 2003 *J. Appl. Phys.* **93** 251
- [23] Stanek C R, McClellan K J, Uberuaga B P, Sickafus K E, Levy M R and Grimes R W 2007 *Phys. Rev. B* **75** 134101
- [24] Eyring L and Baenziger N C 1962 *J. Appl. Phys.* **33** 428
- [25] Schaefer A, Schroeder T, Lupina G, Borchert Y, Dabrowski J, Wenger C and Bäumer M 2007 *Surf. Sci.* **601** 1473
- [26] Seifarth O *et al* 2010 *J. Appl. Phys.* in preparation
- [27] Schroeder T, Zaumseil P, Weidner G, Lupina G, Wenger C and Müssig H-J 2005 *J. Appl. Phys.* **98** 123513
- [28] Mermoux M, Crisci A, Baillet F, Destefanis V, Rouchon D, Papon A M and Hartmann J M 2010 *J. Appl. Phys.* **107** 013512
- [29] Wilke A, Yang J-M, Kim J W, Seifarth O, Dietrich B, Giussani A, Zaumseil P, Storck P and Schroeder T 2010 *Surf. Interface Anal.* <http://dx.doi.org/10.1002/sia.3643>
- [30] Liu J P, Zaumseil P, Bugiel E and Osten H J 2001 *Appl. Phys. Lett.* **79** 671
- [31] Tarsa E J and Speck J S 1993 *Appl. Phys. Lett.* **63** 539
- [32] Williamson G K and Hall W H 1953 *Acta Metall.* **1** 22
- [33] Fathauer R W, Lewis N, Hall E L and Schowalter L J 1986 *J. Appl. Phys.* **60** 3886
- [34] Schroeder T, Giussani A, Dabrowski J, Zaumseil P, Müssig H-J, Seifarth O and Storck P 2009 *Phys. Status Solidi c* **6** 653
- [35] Boscherini F 2008 XAFS The study of semiconductor heterostructures and nanostructures *Characterization of Semiconductor Heterostructures and Nanostructures* ed C Lamberti (Amsterdam: Elsevier) pp 289–330
- [36] Malvestuto M, Carboni R, Boscherini F, d’Acapito F, Spiga S, Fanciulli M, Dimoulas A, Vellianitis G and Mavrou G 2005 *Phys. Rev. B* **71** 075318
- [37] Malvestuto M, Scarel G, Wiemer C, Fanciulli M, D’Acapito F and Boscherini F 2006 *Nucl. Instrum. Methods B* **246** 90
- [38] Birkholz M 2006 *Thin Film Analysis by X-ray Scattering* (Weinheim: Wiley-VCH)